

Contents

6	Overview of the MiniBooNE Detector	1
6.1	Overview of the MiniBooNE Detector Hardware	1
6.1.1	The nuclear target: MiniBooNE mineral oil	3
6.1.2	The optical readout: MiniBooNE photomultiplier tubes	4
6.1.3	Data acquisition system and trigger	5
6.1.4	Calibration devices	8
6.2	The MiniBooNE detector response	11
6.2.1	Light production	11
6.2.2	Light transmission	15
6.2.3	PMT/DAQ response, and hit-level detector calibration	17
6.3	Reconstruction and particle identification algorithms in MiniBooNE .	25
6.3.1	Event reconstruction	25
6.3.2	Reconstruction-level detector calibration and validation	29
6.3.3	Particle identification	30
	Bibliography	34

Chapter 6

Overview of the MiniBooNE Detector

6.1 Overview of the MiniBooNE Detector Hardware

The MiniBooNE neutrino detector consists of a carbon steel spherical tank of 6.1 m in radius and filled with approximately 800 tons of undoped mineral oil. The center of the detector is located at a distance of 541 m from the neutrino production target, below a dirt overburden of about 3 m. Schematics of the MiniBooNE site plan and of the MiniBooNE detector enclosure are shown in Figs. 6.1 and 6.2, respectively.

Neutrino interactions in the oil are observed by detecting the Cherenkov and scintillation photons produced by neutrino-induced charged tracks travelling in the detector medium. An array of 1,280 photomultiplier tubes (PMTs), located at a radius of 5.75 m and oriented towards the center of the tank, is used to record the number and arrival time of the photons produced in the fiducial volume of the detector. The PMTs provide a uniform, 10% coverage of the whole detector spherical inner surface. The spherical detector shell at $5.75 \text{ m} < r < 6.1 \text{ m}$ is optically isolated from the main

This technical cross-section drawing illustrates the internal layout of a building. In the basement, a large spherical storage tank is supported by four vertical pillars. A horizontal pipe with a valve runs along the bottom of the tank. Above the tank, on the upper floor, is a control room or laboratory containing various pieces of equipment, including a large rectangular unit, a smaller box, and a control console with a dial. The building's roof is shown with a gabled structure, and the walls and floor are indicated by hatching lines.

Figure 6.2: *Schematic of the MiniBooNE detector enclosure, showing the vault containing the sperical detector, the electronics/uilities area located above the detector, and the dirt overburden.*

detector region, and serves as a veto region to reject cosmic-ray induced activity in the tank. Photons produced in the veto region are read out by 241 PMTs of the same type employed in the main detector region. The photoelectron charge and time of the PMT signals are continuously digitized and recorded for every proton beam spill. A laser system, a cosmic ray muon hodoscope, and seven scintillation cubes located inside the detector, are used to calibrate various aspects of the MiniBooNE detector response. Hardware details related the MiniBooNE mineral oil, PMT readout, data acquisition system, trigger, and calibration devices follow. More details can be found in [2].

6.1.1 The nuclear target: MiniBooNE mineral oil

Neutrino interactions in MiniBooNE proceed primarily via interactions with mineral oil, since the 810 tons of oil filling the detector comprise about 95% of the total detector tonnage. The remaining 5% detector tonnage consists of the 1 cm thick steel spherical tank, the optical barrier supporting the PMTs, the PMTs themselves, and cables. The interactions from nuclear targets other than mineral oil in the detector, and from the dirt surrounding the detector, are negligible once a fiducial volume requirement is applied to study muon neutrino, charged-current quasi-elastic interactions (see next Chapter).

The mineral oil used in MiniBooNE is Marcol 7, manufactured by Exxon/Mobil. This oil was chosen for its long light attenuation length, high index of refraction and small dispersion over the wavelength range 320-600 nm, its low viscosity, its low reactivity with materials in the detector, and its small amount of scintillation light production. The Marcol oil density is 0.855 g/cm^3 . Details on the mineral oil optical properties of relevance to the MiniBooNE detector response are given in Sections 6.2.1 and 6.2.2.

The oil is kept at ambient temperature. An overflow tank with a capacity of 1%

of the main tank volume is used for oil containment following thermal expansion. The oil can be recirculated and cooled at a rate of about 100 liters per minute, if necessary. Moreover, nitrogen gas can be continuously bubbled into the detector to remove oxygen impurities in the oil, and therefore maintain its optimal optical characteristics over time.

6.1.2 The optical readout: MiniBooNE photomultiplier tubes

The light produced by neutrino interactions is detected by 1,521 photomultiplier tubes. All main and veto tubes are mounted on a spherical support structure built within the detector, at a radius of 5.75 m. Figure 6.3 shows a picture of the actual installation of main and veto PMTs on the detector optical barrier, prior to oil filling.

One thousand, one hundred and ninetyseven of the PMTs installed in MiniBooNE are Hamamatsu R1408 recycled from the LSND experiment, and 324 are Hamamatsu R5912 that were newly purchased for the experiment. Both PMT models have a photocathode diameter of 20 cm. All R5912 PMTs, and the LSND R1408 PMTs offering the best performances, are mounted in the main detection region. Figure 6.4 shows a schematic of a MiniBooNE PMT with its mounting structure for one of the 1,280 main PMTs. The R1408 (R5912) tubes have a 9 (10) stage dynode chain amplification. The PMTs are operated at an average high voltage of about 1,800 Volts. The operating voltage is set separately for each tube, to ensure a uniform gain throughout the tank of $1.6 \cdot 10^7$, as dictated by MiniBooNE electronics. Typical dark noise rates of 3 kHz for the MiniBooNE PMTs have been measured at ambient temperature and default operating voltages, low enough to satisfy the experiment's needs. Some aspects of the PMT response that are of relevance to the event reconstruction are given in Section 6.2.3.

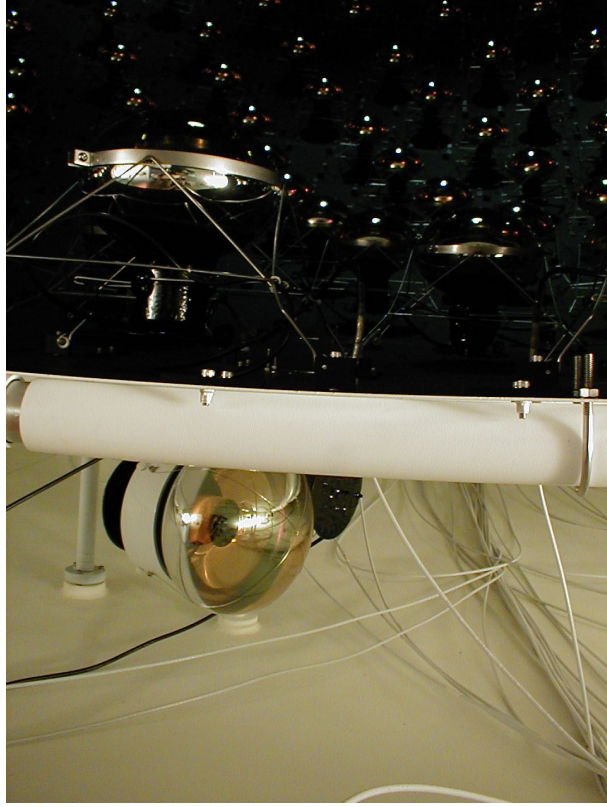


Figure 6.3: *Picture of the MiniBooNE detector optical barrier and its PMT installation, before the detector was filled with mineral oil. The inner and outer surfaces are painted in black and white, respectively, to minimize and maximize light reflection.*

6.1.3 Data acquisition system and trigger

The PMT signals are routed to the electronics area located above the detector, where further amplification and digitization occurs. As for the PMTs, the electronics employed in MiniBooNE is also based on existing LSND hardware, modified to fit the different needs of the experiment.

Because of the high number of channels and the DAQ rate requirements, a full digitization of the PMT signal waveforms is not performed; rather, only the overall charge and time associated with each PMT hit is recorded. A schematic of the charge and time signal formation is shown in Fig. 6.5. The preamplified PMT signals V_{pmt} are continuously integrated via a capacitive circuit contained in the MiniBooNE “QT

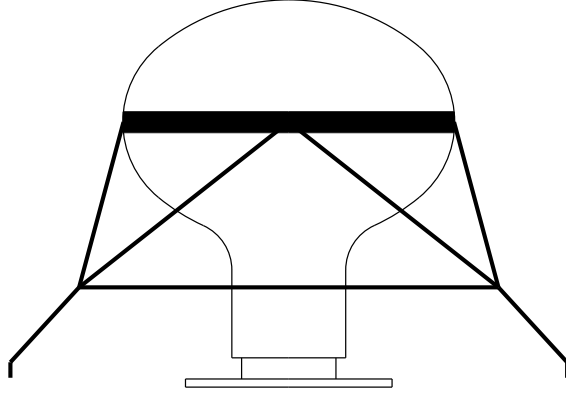


Figure 6.4: *Schematic of a MiniBooNE PMT, together with its support frame used for installation in the MiniBooNE main detection region. To give a sense of scale, the diameter of the photocathode is about 20 cm.*

boards”, with an exponential decay time of about 1,200 ns, generating a second signal V_q . The QT boards (as in “charge/time boards”) serve eight PMT channels each, and are arranged into twelve QT crates each hosting 16 QT boards, for a total of $12 \times 16 \times 8 = 1,536$ channels, enough to serve all the 1,521 MiniBooNE PMTs. The charge signal V_q is continuously digitized by the DAQ, every 100 ns clock ticks. If the PMT signal V_{pmt} exceeds a voltage corresponding to about 0.25 photoelectrons, a PMT discriminator signal is activated, and a linear time ramp V_t is started. The time signal V_t is also continuously digitized every 100 ns. The purpose of the voltage time ramp is to obtain a precise determination of the time at which the PMT signal crosses threshold, since much better than 100 ns time accuracy is necessary for MiniBooNE event reconstruction. The time ramp is reset to baseline two clock ticks after the PMT signal crosses threshold.

The trigger logic is designed to decide whether or not to capture a fixed DAQ time window of PMT charge and time data for all PMTs. The trigger queries the status of several trigger conditions to make this decision. Some trigger conditions use

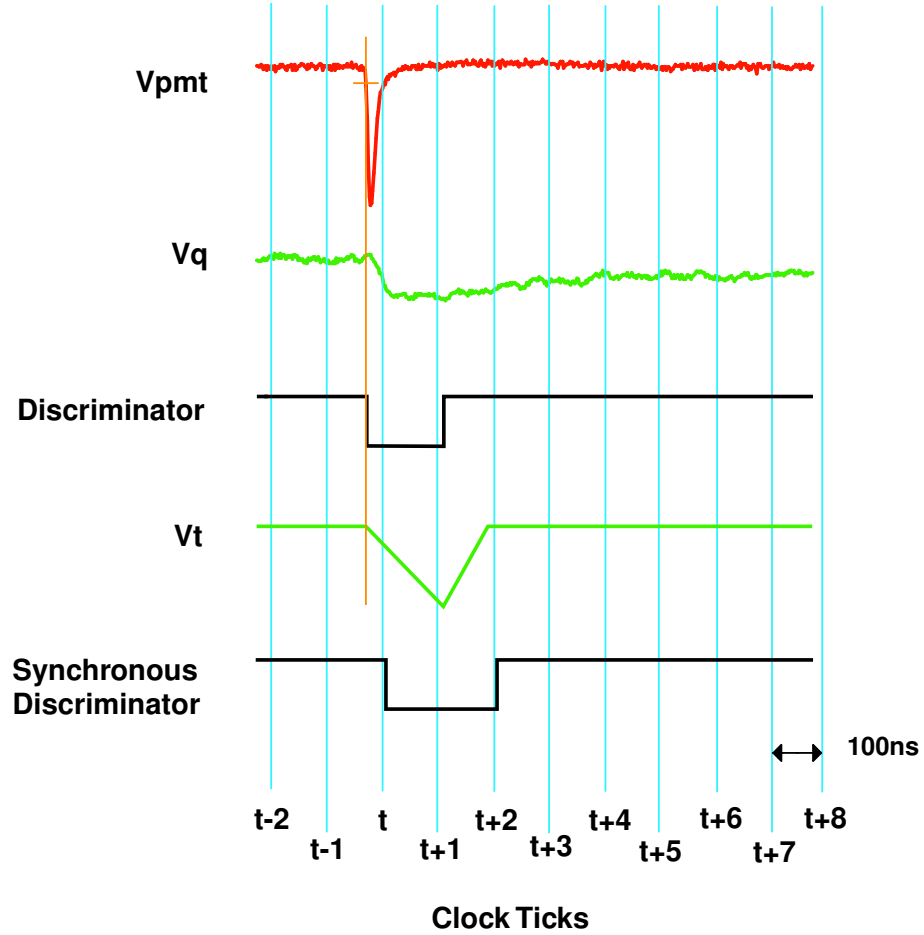


Figure 6.5: *Schematic of the PMT charge and time digitization in MiniBooNE.*

detector data only, for example requiring a minimum number of PMT signals above threshold in the main detector region. However, the most important trigger condition is enabled whenever protons are delivered from the Fermilab Booster accelerator to the MiniBooNE target hall, regardless of the detector status. All neutrino-induced events described in the following are selected based on this trigger condition. The time window captured by this beam trigger is $19.2 \mu s$ long, timed such that the $1.6 \mu s$ long beam spill occurs at $4.6 < \Delta t (\mu s) < 6.2$, where Δt is the time with respect to the beginning of the time window. The duration of the time window is chosen to be able to detect the electrons from muons decaying at rest in the detector with virtually 100% probability. Other important external trigger conditions are set up for detector

calibration (discussed in Sections 6.1.4 and 6.3.2), and for detecting random windows in time to study the detector activity in an unbiased way.

Whenever a trigger condition is met, an event with the following information is recorded for each PMT channel: the clocktick number that preceeds the discriminator firing (the one corresponding to the $(t - 1)$ time in Fig. 6.5), four digitized V_q values, and the corresponding four digitized V_t values, the one that preceeds the discriminator firing, and the three subsequent ones. In addition, in the rare occurrence that high charge PMT hits exceed the charge ADC dynamic range of about 20 PEs, a variation on the DAQ scheme described above is adopted to fully retrieve the PMT charge information.

This digitization scheme allows to recover the intrinsic charge and time resolution of the PMTs, without introducing any additional smearing associated with the data acquisition itself. Some aspects of the digitization process that are of relevance to the event reconstruction are given in Section 6.2.3.

6.1.4 Calibration devices

The MiniBooNE detector is equipped with two systems for its hit-level and reconstruction-level calibration, discussed in Sections 6.2.3 and 6.3.2, respectively. These two calibration systems complement the reconstruction-level calibration samples that can be extracted using MiniBooNE detector information only.

Laser/flask system

A diode laser located in the detector electronics area can deliver sub-ns light pulses into the detector. The laser light wavelength can be set to either 397 nm, or 438 nm; the laser light intensity and repetition rate are adjustable, and of the order of $\mathcal{O}(\mu W)$ and $\mathcal{O}(Hz)$, respectively. The light is transmitted from the laser to the detector via five optical fibers. Four optical fibers are terminated with flasks filled with dispersive

material, yielding a nearly isotropic laser light emission from the flasks. The four flasks are located at various positions within the detector, with one flask positioned at the detector center. The fifth optical fiber is not coupled to a dispersive flask, and yields a collimated ($\sim 10^\circ$ opening angle) beam of laser light in the mineral oil. A special calibration trigger enables to record the detector activity following laser light calibration events, which occur off-time with respect to the proton beam delivery to the MiniBooNE target hall. As described in Section 6.2.3, laser events allow to calibrate the individual PMT responses.

Cosmic ray muon tracker and scintillation cubes

Cosmic ray muons and their decay electrons provide extremely useful event samples for calibrating the detector as a whole, at the reconstruction-level (see Section 6.3.2). The cosmic ray muon hodoscope located above the detector and the scintillation cubes located inside the detector allow to record the detector activity due to muons with known direction, and with known pathlength and energy deposition inside the detector.

The cosmic ray muon hodoscope consists of four scintillator planes, spatially separated into two layers of two planes each. The muon tracker trigger is enabled by a 4-fold scintillator plane time coincidence. In a coordinate system where \vec{y} points upwards and \vec{z} along the neutrino beam direction, the two layers are separated by $\Delta y \equiv y_{top} - y_{bottom} \simeq 100$ cm. The two planes of scintillator strips in each layer are oriented to provide one (x, y) and one (y, z) 2-dim coordinate, therefore providing a full 3-dimensional location. From the top and bottom layer 3-dimensional coordinates, the muon track direction and entry point inside the detector can be extracted. The muon tracker dimensions and location with respect to the detector allow to calibrate the detector track direction reconstruction algorithms over the the range $-1 < \cos \theta_y < \cos \theta_{y,max}$, $-\sqrt{1 - \cos^2 \theta_{y,max}} < \cos \theta_x, \cos \theta_z < \sqrt{1 - \cos^2 \theta_{y,max}}$, where $\cos \theta_x, \cos \theta_y, \cos \theta_z$ are the direction cosines of the muon track direction ($\cos \theta_y = -1$

for downward-going muons), and $\cos \theta_{y,max} \simeq -0.65$. Moreover, the muon tracker scintillator strip segmentation and location yields an angular resolution intrinsic to the tracker of about 30 mrad, which is smaller than the typical 100 mrad angular spread expected for multiple Coulomb scattering of muons in the detector [3].

Seven optically isolated cubes, made of scintillator material and of a few cm on a side, are deployed inside the MiniBooNE detector. The scintillation light produced by a charged particle moving inside a cube is collected by an optical fiber, and directed to a 1 inch PMT located outside the detector. The cube trigger is enabled whenever a time-delayed coincidence between two light pulses from the same cube are detected by the PMT readout, consistent with an event having a muon reaching and stopping inside a cube (first light pulse), followed by a second scintillation light pulse produced by the muon decay electron along its path inside the cube. Therefore, cube events allow to determine the stopping position of a muon inside the MiniBooNE detector to a few cm accuracy, including the cube survey position accuracy. The cubes are located at various positions inside the detector, so that the distances between the cubes and the detector surface range from 15 to about 400 cm. Given the energy loss of muons in oil, the cube positions allow to study muons that deposit between 20 and 800 MeV of energy inside the tank [4].

The coincidence between a muon tracker trigger signal and a scintillation cube trigger select muons with known direction and entry point position (from the tracker), and known stopping point (from the cube); from the entry and stopping points, the muon pathlength and the energy deposition inside the detector are determined. On an event-by-event basis, the muon energy resolution measured by the tracker/cube calibration system is dominated by the few % fluctuations in energy loss (range straggling).

6.2 The MiniBooNE detector response

6.2.1 Light production

Optical photons ¹ are produced in the mineral oil by charged tracks via the mechanisms of Cherenkov and scintillation light production.

Cherenkov light

Cherenkov light production in a dispersive medium with index of refraction n , by a relativistic particle of charge ze and moving at a velocity $\beta > 1/n$, is given by [1]:

$$\frac{d^2N}{dx d\lambda} = \frac{2\pi\alpha z^2}{\lambda^2} \sin^2 \theta_C \quad (6.1)$$

where $d^2N/dxd\lambda$ is the number of Cherenkov photons emitted per particle's unit path length x and per unit photon wavelength λ , $\alpha = e^2/(\hbar c)$, and θ_C is the angle of Cherenkov light emission with respect to the particle's direction, given by:

$$\cos \theta_C = \frac{1}{\beta n(\lambda)} \quad (6.2)$$

The refractive index n of the MiniBooNE mineral oil at a temperature of 20 degC has been measured to be [5]:

$$n(\lambda) = n_D + B\left(\frac{1}{\lambda^2} - \frac{1}{\lambda_D^2}\right) \quad (6.3)$$

with λ being the photon wavelength in nm, $\lambda_D = 589.3$, $n_D = 1.4684 \pm 0.0002$, and $B = (4240 \pm 157) \text{ nm}^2$.

As the particle slows down (decreasing β), Cherenkov light is emitted at smaller angles θ_C , and the number N of Cherenkov photons produced decreases. Cherenkov light production is absent if $\beta < 1/n(\lambda)$. The MiniBooNE detector is sensitive to optical photon production in the $250 < \lambda(\text{nm}) < 650$ range only; the Cherenkov flux

¹We define here optical photons as photons in the $250 < \lambda (\text{nm}) < 650$ wavelength range.

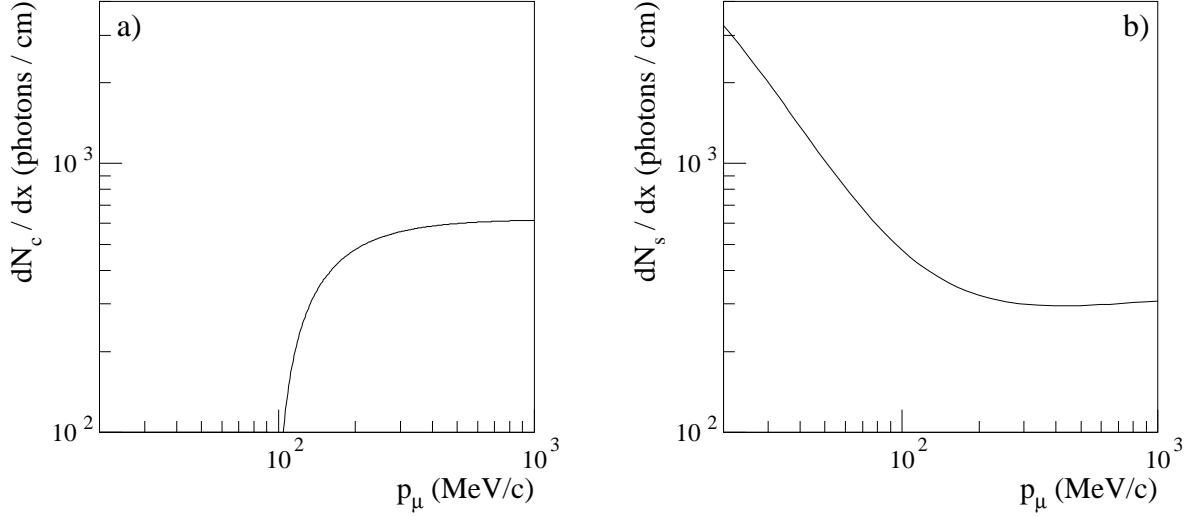


Figure 6.6: *Number of optical photons produced per unit path length of muons in MiniBooNE mineral oil, as a function of muon momentum p_μ . Figure 6.6a) shows Cherenkov light production per unit path length, dN_c/dx , integrated over the photon wavelength range $250 < \lambda(\text{nm}) < 650$. Figure 6.6b) shows scintillation light production per unit path length, dN_s/dx , integrated over the whole scintillation emission spectrum.*

yield per unit track length for muons, integrated over this wavelength range and as a function of the muon momentum p_μ , is shown in Fig. 6.6a).

A typical 300 MeV/c muon produces about 560 Cherenkov photons per cm in mineral oil, in the $250 < \lambda(\text{nm}) < 650$ photon wavelength range. For this muon momentum and in this photon wavelength range, the mean and RMS of the photon wavelength spectrum are 385 nm and 109 nm, respectively; as discussed Sections 6.2.2 and 6.2.3, the Cherenkov emission spectrum matches well the photon wavelength range of the MiniBooNE detector response. Moreover, the mean and RMS of the cosine of the Cherenkov angle in the same photon wavelength range $250 < \lambda(\text{nm}) < 650$ and for the same muon momentum of 300 MeV/c are 0.711 and 0.008, respectively; the angular distribution of Cherenkov emission is anisotropic. Finally, the Cherenkov light emission is prompt.

Scintillation and fluorescence light

Charged tracks traversing mineral oil excite the target molecules because of energy deposition; the following de-excitation of the mineral oil organic molecules is accompanied by isotropic and delayed scintillation light emission. The emission wavelength spectrum and the emission time spectrum of scintillation light depends on the details of the mineral oil chemical composition and molecular structure, and are determined experimentally. A related process is the excitation of target molecules by optical photons (as opposed to charged tracks); the following de-excitation of mineral oil molecules is accompanied by fluorescence light emission. In both cases, several fluorophores contribute to the light emission.

Scintillation and fluorescence light are only approximately proportional to the ionization loss of tracks in mineral oil, and recombination and quenching effects are believed to reduce the light yield for highly ionizing particles. The semi-empirical Birk's saturation law for energy deposition is typically used to convert the ionization energy loss per unit path length and unit material density, dE/dx ($MeV/(g\ cm^{-2})$), into a corrected energy loss dE'/dx that is directly proportional to the light output [1]:

$$dE'/dx = \frac{dE/dx}{1 + k_B dE/dx} \quad (6.4)$$

where the Birk's constant k_B is about $0.014\ g\ cm^{-2}$ for mineral oil.

The properties of scintillation light production are determined empirically, both from external measurements and from MiniBooNE detector data. The identification of the mineral oil fluorophores, the decay time constant of their exponential light emission, and their wavelength emission spectra, are determined from external measurement on time resolved fluorescence [6]. The light yield per energy deposited for each fluorophore is determined both from these external measurements, and from MiniBooNE detector calibration data using electrons from muon decays at rest. These properties are summarized in Tab. 6.1.

Fluorophore	dN_s/dE' (photons/MeV)	τ (ns)	Emission Spectrum	
			Mean(λ) (nm)	RMS(λ) (nm)
1	82.8	14.0	303	13
2	68.4	33.0	360	27
3	19.8	1.0	331	18
Total	171.0			

Table 6.1: *Properties of scintillation light emission spectra in MiniBooNE mineral oil. The properties of the three dominant fluorophores are listed. dN_s/dE' is the number of scintillation photons emitted per unit energy deposition, where the energy deposition is corrected for Birk's saturation law (see text for details); τ is the decay time constant of the exponential time distribution of the emitted light; Mean(λ) and RMS(λ) are the mean and RMS of the emission wavelength spectrum, respectively.*

The total scintillation light yield per unit path length, for a muon travelling in mineral oil, is given in Fig. 6.6b) as a function of muon momentum. A typical 300 MeV/c muon produces about 300 scintillation photons per cm in mineral oil, integrated over the entire photon emission spectrum. $270 < \lambda \text{ (nm)} < 460$. The typical photon wavelengths characterizing scintillation emission spectra for the various mineral oil fluorophores are shorter than the corresponding ones associated with Cherenkov light emission, and therefore scintillation photons do not match equally well the photon wavelength range of the MiniBooNE detector response; consequently, the typical $560 : 300 \sim 2 : 1$ ratio between Cherenkov and scintillation photons at production is translated in a larger ratio at detection. As already mentioned, scintillation light production is isotropic and characterized by delay times of the order of tens of ns (see Tab. 6.1).

6.2.2 Light transmission

Optical photons typically have to traverse distances of the order of a few meters before reaching a PMT located on the optical barrier surface, and therefore be detected. Light propagation over distance is affected mainly by three physics processes: photon absorption, scattering, and fluorescence. The term “photon attenuation” is used here to describe these three physics process cumulatively, and it is to be interpreted as the attenuation of photons measured along the direction specified by their initial direction at production. The individual absorption, scattering, and fluorescence rates, together with the overall attenuation rate, are shown in Fig. 6.7 as a function of the photon wavelength. The attenuation rate is defined as the number of photon interactions resulting in attenuation (as specified above) per unit path length. For typical photon wavelengths of 400 nm, the attenuation rate is $R_{att} \simeq 7 \cdot 10^{-4} \text{ cm}^{-1}$, corresponding to an attenuation length of $L_{att} \simeq 1/R_{att} \simeq 14 \text{ m}$, that is of the order of the MiniBooNE detector diameter [6]. For the same wavelength of 400 nm, about half of the attenuation is interpreted as due to absorption, and half as due to scattering.

Fluorescence

Fluorescence is the process in which an optical photon (created by either Cherenkov or scintillation light production processes) is absorbed by the mineral oil in the form of molecular excitation, and re-emitted at a longer wavelength, different direction, some time after absorption. Fluorescence measurements using samples of MiniBooNE mineral oil were carried out both at Johns Hopkins University and at Fermilab [6]. The emission spectra of fluorescent light have already been discussed in connection to scintillation light production. The measured relationship between absorption and emission spectra for the mineral oil fluorophores is typically characterized by Stokes’

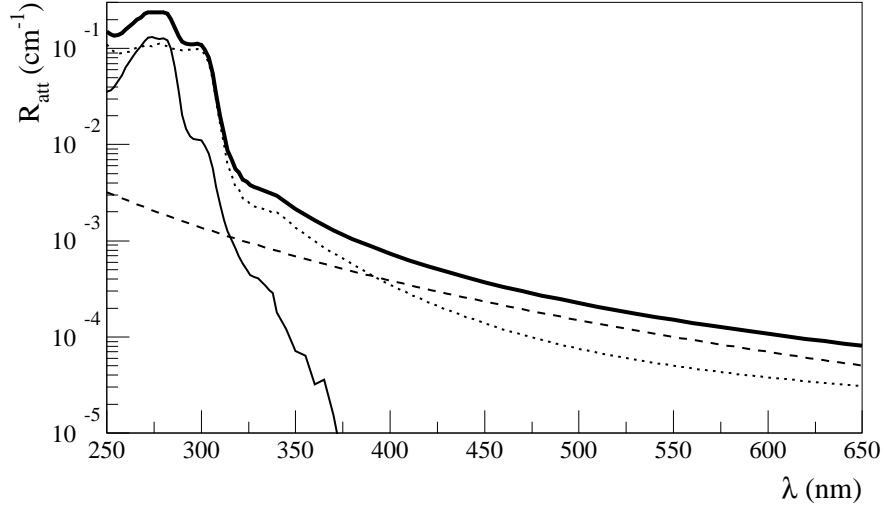


Figure 6.7: The attenuation rate R_{att} in MiniBooNE mineral oil as a function of photon wavelength λ is shown by the thick, solid curve. The individual components to the attenuation rate are also shown: fluorescence rate (thin, solid line), scattering rate (dashed line), absorption rate (dotted line).

shifts of a few tens of nm, where the Stokes' shift refers to the wavelength difference between the peak of the absorption and emission spectra. The measured contribution of fluorescence to attenuation becomes significant only for photon wavelengths below about 300 nm; in this case, photons with longer wavelengths (and therefore subject to smaller attenuation rates) are emitted.

Scattering

Scattering is defined here as the process in which an optical photon interacts with target molecules, gets deflected and possibly changes its polarization state, but not its wavelength. Scattering measurements of photons in mineral oil were carried out at Princeton University [7]. The dominant contribution to scattering is measured to be due to isotropic Rayleigh scattering, although also anisotropic Rayleigh scattering and Raman scattering are observed, contributing to roughly 20% and 7% of the total scattering rate, respectively. All scattering rate components approximately decrease

as λ^{-4} with increasing photon wavelength λ .

Absorption

Photon attenuation in mineral oil, due to either fluorescent emission, scattering, or absorption, was measured at Fermilab with different experimental setups and over a wide photon wavelength range [6]. The difference between the attenuation rate curve as a function of wavelength obtained by these measurements on the one hand, and the sum of the fluorescence and scattering rates discussed above on the other, is interpreted as photon absorption in mineral oil.

6.2.3 PMT/DAQ response, and hit-level detector calibration

Having described the production and transmission of optical photons to the PMT surface, we are left with the description of the PMT/DAQ charge and time response.

Charge response

The charge response can be classified into three parts: photocathode response, charge collection response, and charge digitization. The photocathode response is described by the quantum efficiency, that is the probability to convert one photon of wavelength λ into one photoelectron at the photocathode surface. The quantum efficiency as a function of photon wavelength λ is shown in Fig. 6.8a), for both R1408 and R5912 PMTs [8]. For both types of PMTs, the quantum efficiency peaks at around $\lambda = 400$ nm; moreover, the quantum efficiency of R1408 PMTs is about 15% lower than the R5912 PMT quantum efficiency over all wavelengths.

The charge collection response is determined by the photocathode geometry (shown in Fig. 6.4), the incident light spatial and angular distribution on the mineral oil/photocathode boundary, and by details of photon and electron transport at the

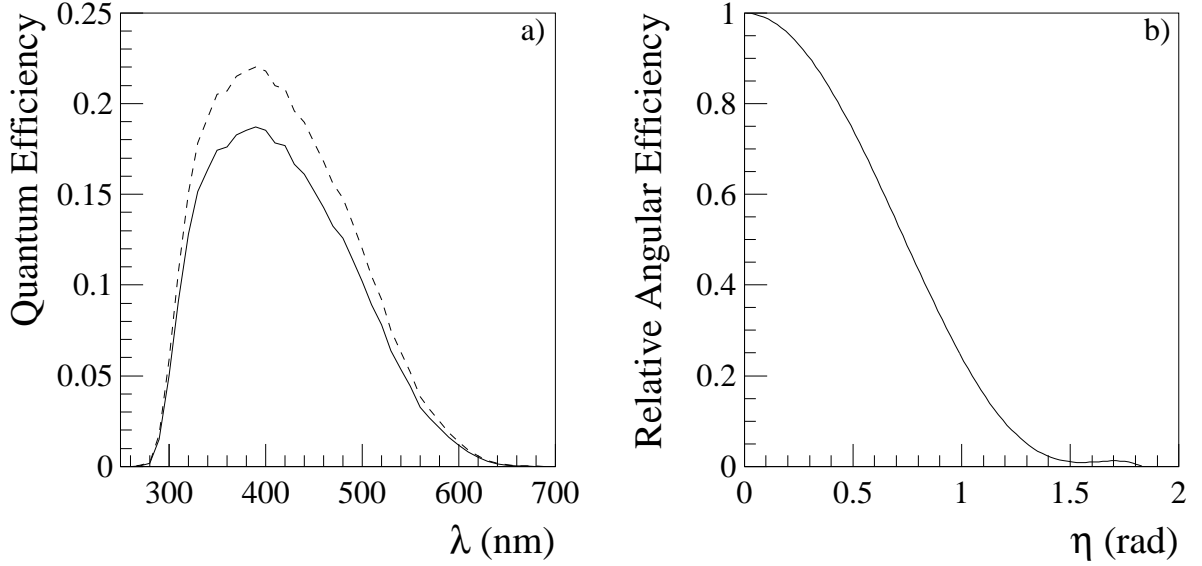


Figure 6.8: *Quantum efficiency and angular response for MiniBooNE PMTs. Figure 6.8a) shows the quantum efficiency as a function of incident photon wavelength λ , for R1408 (solid curve) and R5912 (dashed curve) PMTs. Figure 6.8b) shows the angular efficiency for both R1408 and R5912 PMTs, where η indicates the angle between the direction of a broad beam of light and the PMT symmetry axis, relative to the efficiency for light hitting the PMTs head-on ($\eta = 0$).*

photocathode and through the PMT dynode chain. The charge collection angular response has been measured by immersing the PMTs in mineral oil, and by illuminating their photocathode surface with an intense, broad, parallel beam of light, for various angles η between the photon beam and the PMT symmetry axis (head-on light for $\eta = 0$). The results are shown in Fig. 6.8b), normalized to the $\eta = 0$ response. The dominant effect in Fig. 6.8b) is the solid angle subtended by the photocathode surface with respect to the beam of light; since R1408 and R5912 PMT photocathode geometry is the same, the curve in Fig. 6.8b) is approximately applicable to both types of PMTs.

The details of electron transport through the PMT dynode chain determines the PMT charge resolution, that is the probability to measure an amount of charge q for

a given amount μ of photoelectron charge created at the photocathode. Photomultipliers of type R1408 and R5912 have a different dynode structure, leading to different charge collection responses. The charge resolution is measured via the MiniBooNE laser/flask calibration system, using the charge digitization scheme described in Section 6.1.3. Therefore, the PMT charge calibration relating the charge ADC values to number of photoelectrons is described first.

The charge calibration [9] is extracted by directing very low levels of light to the laser central flask, located at the same distance with respect to all MiniBooNE PMTs. The light level and flask/PMT distance chosen ensure that, to a very good approximation, each PMT is hit by at most one photon for every laser light pulse. The PMT charge calibration can be extracted, individually for each PMT, by requiring that $\langle q \rangle = 1$ PE, where the average is intended over a large number of hits with nonzero charge. More specifically, calibrated charges q are extracted from ADC values via:

$$q [PE] = \frac{V_q [ADC]}{g_q [ADC/PE]} \quad (6.5)$$

where g_q are calibration constants converting ADC counts to number of photoelectrons, while $V_q [ADC]$ is a function using the four digitized charge ADC values to obtain the total PMT integrated charge, in ADC counts. The calibration constants g_q are different for each PMT channel, to account for different PMT gains, preamplifier gains, and different PMT dynode structures. The function V_q is common to all PMTs of the same type (R1408 or R5912), but different for the two types of PMTs, to account for the different PMT signal shapes.

Having briefly defined the PMT charge calibration procedure, we can discuss the PMT charge resolution on a hit-by-hit basis [citeboonetn126,boonetn100](#). The PMT charge resolution plays an important role in the accuracy of the MiniBooNE energy reconstruction. The probability to measure a calibrated charge q given a predicted amount μ of charge is shown in Fig. 6.9, for both R1408 and R5912 PMTs, and for typical PMT charges of $\mu = 1$ and 5 photoelectrons. Typical charge resolutions for R1408 (R5912) PMTs are about 1.5 (1) PEs for $\mu = 1$ photoelectrons, and 4 (3)

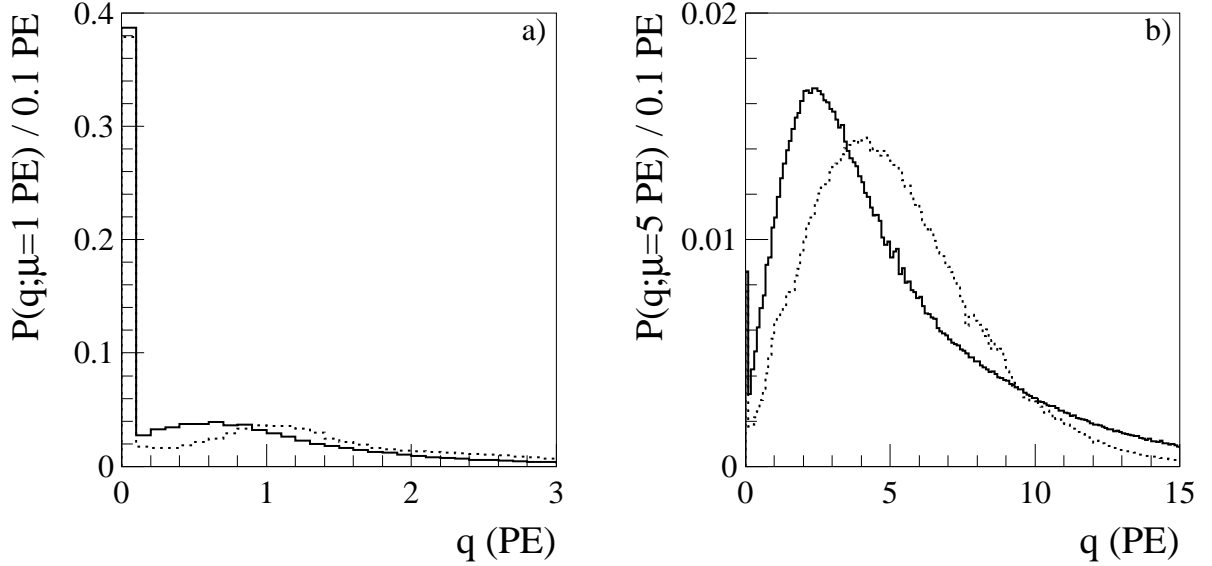


Figure 6.9: *PMT charge response to $\mu = 1$ PE (panel a)) and $\mu = 5$ PE (panel b)) levels of illumination for MiniBooNE PMTs. The response of R1408 (LSND) PMTs is shown with solid histograms; the response of R5912 (new) PMTs is shown with dotted histograms.*

PEs for $\mu = 5$ photoelectrons, where the resolution is defined here as the RMS of the distributions shown in Fig. 6.9. This charge resolution is sufficient for obtaining a satisfactory energy reconstruction, given the large number of PMT hits in a typical neutrino interaction: for example, muon neutrino charged-current, quasi-elastic neutrino interactions reconstructed in MiniBooNE have a mean number of PMT hits in the main detector region of about 500, and a mean charge per PMT hit of about 3 photoelectrons.

The procedure used to extract the charge resolution functions shown in Fig. 6.9 also use the laser/flask system, this time over a wide range of laser light intensity and a wide range of laser flask / PMT distances. The curves are normalized to unity, $\int dq P(q; \mu) = 1$. Laser events, as well as neutrino-induced events, can be reconstructed in MiniBooNE. The reconstruction algorithm used in this case to predict the amount of PMT charge μ , at least up to a normalization constant, is based not only on the light transmission (Section 6.2.2) and PMT response (this Section) properties

described above, but also on the known laser light production characteristics (wavelength and position of light source, angular distribution of emitted light, etc.). The normalization constant for a given light intensity is determined via $\langle \mu \rangle_{q>0} = \langle q \rangle_{q>0}$, where the average is over all non-zero charge PMT hits. Based on the PMT charge prediction, it is possible to predict the fraction of events in which no photocathode charge is created, and therefore extract the full charge resolution function including the $q = 0$ case, also shown in the distributions in Fig. 6.9. These histograms include the effects due to the digitization threshold of approximately 0.25 PE, and PMT hits corresponding to a charge below threshold are given in the $q = 0$ bin. Two charge resolution functions are obtained with laser data, one for R1408 PMTs, and one for R5912 PMTs. The charge response $P(q; \mu)$ described above forms the basis of the charge likelihood part of the MiniBooNE maximum likelihood event reconstruction discussed in Section 6.3.1.

Time response

As for the charge response, the time response also depends both on details related to the PMT charge collection mechanisms, and on the DAQ digitization algorithm used in MiniBooNE. Moreover, the time response is also affected by the intrinsic time delays associated with scintillation and fluorescence light production, and scattering. As for the charge response, we start by describing the PMT time calibration, and then discuss the PMT time resolution.

The time calibration for each of the MiniBooNE PMTs, relating time ADC values to charge collection times, can be extracted with laser events [9]. More specifically, calibrated times t_{corr} , corrected for the photon transit time from the light source to the PMT, are obtained via:

$$t_{corr} = t_{raw}(g_t[ADC/ns]) + t_{offset} - t_0 - |\vec{x}_{pmt} - \vec{x}_0|/c_n \quad (6.6)$$

where the raw time t_{raw} depends on channel-specific time slopes g_t determining the relationship between times in ns and time ADC counts V_t , t_{offset} is a channel-specific time offset accounting for cable length differences and different dynode structures, t_0 is the earliest emission time of photons from the laser flask source, \vec{x}_{pmt} is the known PMT location, \vec{x}_0 is the known laser flask location, and c_n is the known velocity of light in a medium of refractive index n . For laser light, the time distribution $F(t_{emission})$ of light emission has a negligible time width compared to the detector time resolution, and can be taken to be instantaneous: $F(t_{emission}) = \delta(t_{emission} - t_0)$.

The corrected time resolution functions for the MiniBooNE PMTs cannot be entirely extracted from laser events, since tracks in the detector produce delayed scintillation light that cannot be simulated with the laser system, and therefore the time distributions of light emission $F(t_{emission})$ are different in the two cases. For particle tracks in the detector, whose position is generally unknown prior to reconstruction, the PMT corrected time is still described by Eq. 6.6, where t_0 and \vec{x}_0 are now parameters to be determined, referring to the track's earliest light emission time, and track position (see Section 6.3.1).

The corrected time resolution functions assumed by the reconstruction algorithm for three different light detection hypotheses are shown in Fig. 6.10. The examples sgiven refer to 50 MeV electron tracks. We mention here three important features related to the expected corrected time distributions shown in Fig. 6.10:

PMT intrinsic time resolution : from Figs. 6.10a) and b), referring to single-PE hits due to prompt, Cherenkov, light, a typical PMT intrinsic time resolution of the order of 1 ns can be extracted. The time resolution is slightly better for R5912 than for R1408 PMTs. This reconstruction parameter is tuned based on low intensity laser events, by measuring the spread in the PMT hit times [12]. As discussed in Section 6.3.1, the PMT intrinsic time resolution is important for reconstructing the light source position (laser flask or light-emitting particle track) in the detector, and all the reconstructed parameters that depend on the

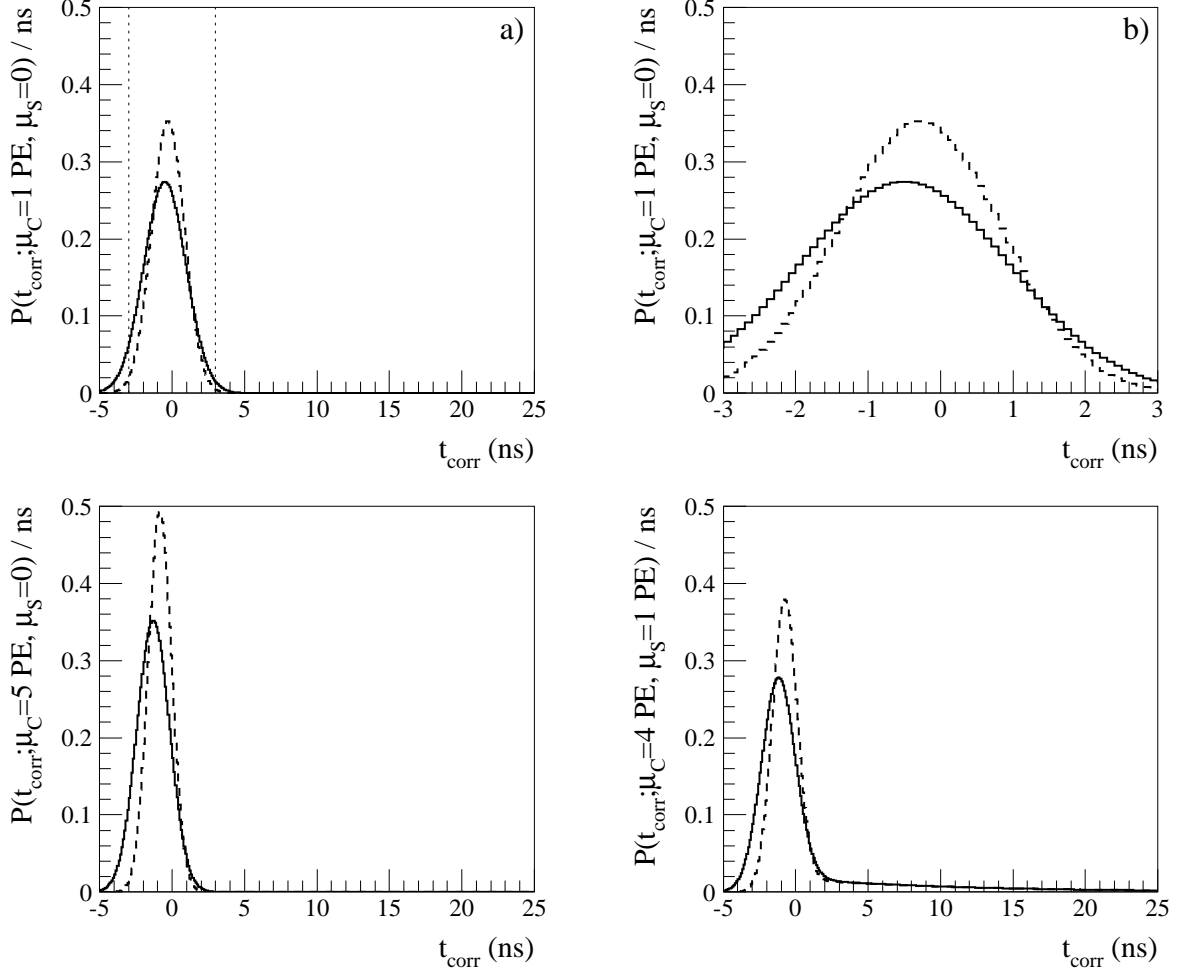


Figure 6.10: *PMT corrected time likelihood for 50 MeV electron events, as used in the MiniBooNE reconstruction algorithms. The response function for R1408 (R5912) PMTs is shown by the solid (dashed) histograms. Figure 6.10a) shows the expected corrected time distributions for PMTs hit by a single Cherenkov photon; Figure 6.10b) is the same as a), but zoomed in the $-3 < t_{\text{corr}} \text{ (ns)} < 3$ time interval; Figures 6.10c) and d) show the corrected time distributions for PMTs hit by five Cherenkov photons, and by four Cherenkov photons plus one scintillation photon, respectively.*

event position. Based on the velocity of light in mineral oil, a time spread of 1 ns approximately corresponds to a 20 cm spread in the reconstructed distance between the light source and the PMT location.

Time slewing and multi-PE hits : the corrected time distributions for 5 PE prompt hits (Fig. 6.10c)) are shifted toward earlier times and are narrower, compared to the 1 PE prompt hits ones (Fig. 6.10a)). This is due to a combination of two effects. First, time slewing, that is the time jitter for a PMT signal to cross the DAQ threshold, is more pronounced for low-charge signals [9]. Second, the MiniBooNE DAQ system records the time of the earliest photoelectron only, even when several photoelectrons are present in a hit. Also this second effect tends to decrease the mean time and width of the corrected time distributions [13]. This feature is measured with laser events as well, using different light levels and laser flask positions.

Delayed light: Figure 6.10d), referring to the corrected time distribution expected for PMT signals due to four Cherenkov photons and one scintillation photon, shows a long exponential tail for large corrected times, with a typical decay time constant of the order of tens of ns. This tail is due to the delayed light emission from scintillation processes. As the time slewing and multi-PE effect, it is coupled to the PMT charge resolution, since the prompt photons can give rise to PMT signals below threshold because of non-zero charge resolution, and therefore the PMT hit time can be determined by the arrival time of the delayed photon. This aspect of the corrected time distribution is tuned based on electron events from muon decays at rest [13]. In this context, the tail at large corrected times is not solely due to scintillation, but also to fluorescence and scattering processes.

In addition to the ones described above, there are other aspects affecting the corrected time distributions. First, higher-energy particle tracks have a light emission pattern which is spatially more extended, and therefore a broader corrected time distribution. This effect is taken into account by the reconstruction algorithms [13]. Second, PMT pre-pulsing, PMT after-pulsing, and light reflections from the black-painted PMT

support structure have been observed with laser events [12], and are taken into account in the detector Monte Carlo simulation; their impact on the reconstruction is expected to be small, and it is neglected in the algorithms that we describe next.

6.3 Reconstruction and particle identification algorithms in MiniBooNE

6.3.1 Event reconstruction

The maximum likelihood event reconstruction in MiniBooNE [13] uses the measured charge and time PMT responses in the MiniBooNE detector to reconstruct the properties of the final state of a neutrino interaction. The algorithms used focus on the three most important types of final state particles that can be observed with the MiniBooNE neutrino beam: electrons, muons, and neutral pions. Electrons from muon decays are reconstructed separately from the prompt part of the neutrino interaction, since the muon decay timescale (of the order of $2\ \mu s$) is much longer than the timescales for light production, propagation and detection in the detector (tens of ns), which ultimately affect the particle reconstruction. The reconstruction categorizes events based on the number of expected Cherenkov rings. Electrons and muons produce a single ring of Cherenkov light in the prompt part of the event (*i.e.*, ignoring muon decay), while $\pi^0 \rightarrow \gamma\gamma$ decays produce two rings, one for each photon conversion in mineral oil. Events can therefore be reconstructed both under a single ring, and a two-ring assumption. This analysis focuses on events with a single muon in the final state, and therefore we discuss below the single Cherenkov ring reconstruction only. Differences between muon and electron/photon Cherenkov rings are briefly discussed in the Section 6.3.3, addressing particle identification. Moreover, there currently exists two independent reconstruction software packages in MiniBooNE; only the one used in this analysis is described below.

For each event with a single Cherenkov track in the final state, the following quantities are reconstructed:

- position and time of the mid-point along the track;
- direction of the track;
- length of the track;
- separate amounta of Cherenkov and scintillation light produced by the track;
- energy of the track.

Given the complexity of the reconstruction algorithms, not all quantities are reconstructed at once. Rather, a step-by-step minimization approach is chosen, in which the sophistication of the model prediction is gradually increased for better reconstruction, and in which the results of the previous minimization step are used as starting point. For muon reconstruction, the four minimization steps used are described below, and summarized in Tab. 6.2. The main building blocks for the time and charge likelihood functions are discussed in Sections 6.2.1, 6.2.2, and 6.2.3, where the emphasis is on hit-level quantities. The reconstruction calibration for global event quantities, such as energy or light fluxes, is discussed in Section 6.3.2.

Step 1: track position, time, direction, and energy from simple time likelihood

First, the approximate position \vec{x}_1 and time t_1 of the mid-point of the muon track are reconstructed (4 parameters), using PMT time information only, based on two generic time likelihood functions for the corrected times defined in Eq. 6.6, depending on the PMT type, *i.e* of type R1408 or R5912. As already mentioned, these time likelihoods have two components: a Cherenkov component for the prompt light, and a scintillation component for the delayed light. Second, the track direction \hat{u}_1 is

determined from a charge-weighted average of the directions defined by the PMT locations with respect to the position \vec{x}_1 , using only the prompt charge detected by the PMTs that measure a non-zero charge. Third, the track energy E_1 is reconstructed, following a parametrisation that depends on the total measured charge Q for the event, and the distance of closest approach between the position \vec{x}_1 and the spherical surface defined by the PMT locations. Fourth, the predicted Cherenkov (ρ) and scintillation (ϕ) light fluxes emitted by the track are computed, assuming that both light fluxes are directly proportional to the reconstructed energy E_1 .

Step 2: track position, time, direction, and energy, from refined time and charge likelihood

First, the accurate position \vec{x}_2 , time t_2 , and direction \hat{u}_2 of the track are reconstructed (6 parameters), using both PMT time and charge information, based on two combined time plus charge likelihood functions, one for each PMT type. The time likelihoods used in this minimization step are more sophisticated than the previous ones, and depend on the reconstructed energy E_1 as well as on the amounts of charge μ predicted by the reconstruction for each PMT, which in turn depend on the energy (E_1), and on the Cherenkov (ρ_1) and scintillation (ϕ_1) light fluxes returned by the first reconstruction step. The dependency of the time likelihood from the predicted charges μ and track energy E is discussed in Section 6.2.3. The charge likelihoods introduced in this step depend on the same three quantities E_1, ρ_1, ϕ_1 . Unlike the time likelihoods, which use only PMTs measuring a non-zero charge, the charge likelihoods use all PMTs, since the probability to measure no charge q_j on a PMT given a certain predicted amount of charge μ_j is a well-defined quantity that can be computed, as also discussed in Section 6.2.3. Second, using the new position \vec{x}_2 , a more accurate estimate of the energy (E_2) is computed, using the same parametrization of step 1. In this minimization step, the Cherenkov and scintillation light fluxes are kept unchanged.

Step 3: Cherenkov and scintillation light fluxes

First, new values for the predicted Cherenkov (ρ_3) and scintillation (ϕ_3) light fluxes are computed (2 parameters), using combined time plus charge likelihood functions similar the ones used in step 2. In this minimization step, the midpoint track position, time, and direction are kept fixed to the values obtained in step 2 of the reconstruction (*i.e.*, $\vec{x}_2, t_2, \hat{u}_2$). Second, an energy estimate that is alternative to the one computed in step 2 is obtained: the reconstructed energy E_3 is based solely on the predicted amount of Cherenkov light ρ_3 in the event. The proportionality constant C_ρ between energy and Cherenkov light flux is the same as the one used in step 1.

Step 4: track length

The track extent (1 parameter) is estimated in this last step. Unlike the previous three steps, the measured PMT times and charges are not assumed to be due to a point-like Cherenkov and scintillation light source in the detector. Rather, the reconstruction assumes two point-like sources, each having half the Cherenkov and scintillation flux strength previously computed. The two sources are assumed to be distributed along the track direction, and equally spaced with respect to the track midpoint. This “symmetry” assumption is motivated by the nearly uniform light emission along the muon track due to both the Cherenkov and scintillation light processes. As shown in Fig. 6.6, this is a reasonable approximation for the part of the muon track above $p_\mu = 200$ MeV/c. A discrete light emission model based on two point-like sources is assumed (as opposed to a continuous light model), to keep the CPU time requirements of the reconstruction algorithm at a manageable level. As for steps 2 and 3, combined time plus charge likelihoods are used in step 4. For the purposes of estimating the track length, the midpoint track position, time, and direction are assumed to be the ones computed in step 2 ($\vec{x}_2, t_2, \hat{u}_2$), while the Cherenkov light flux, scintillation light flux, and track energy are fixed to the values computed in step 3 (ρ_3, ϕ_3, E_3).

6.3.2 Reconstruction-level detector calibration and validation

We now briefly discuss the calibration and validation of global quantities related to the MiniBooNE events.

The accuracy of the light source position reconstruction can be validated with laser events, since the position of the laser flasks is known; typical accuracies of the order of 20 cm are obtained [14].

The accuracy of the track direction reconstruction can be validated with cosmic ray muons passing through the muon tracker, whose direction is known. Directional accuracies of the order of 3 deg are obtained [3].

The track length reconstruction can be calibrated and its accuracy validated with cosmic ray muons passing through the muon tracker and stopping in a scintillation cube, whose track length in the detector is known. The reconstructed length tends to be reconstructed to lower values compared to the actual track length, for tracks lengths exceeding about 2 m. This bias is due to the two-point light source approximation used in determining the track length, which becomes less and less valid as the track length increases, and therefore it is understood. Correcting for this bias, typical accuracies of the order of 10% are obtained [4].

The energy reconstruction is calibrated with electrons from muon decays at rest, whose energy distribution is known, characterized by an endpoint energy of 52.8 MeV. More specifically, this sample is used to determine the functional form for the charge-to-energy conversion $E = E(Q, \vec{x})$ appearing in Tab. 6.2. Moreover, the accuracy of the energy reconstruction can be validated with electron, muon, and neutral pion events. First, the energy resolution obtained for electron events from muon decays at rest at the decay endpoint of 52.8 MeV is about 13% [10]. Second, the energy resolution for cosmic ray muons stopping in scintillation cubes is of the order of 10% [4]. Few percent corrections, based on Monte Carlo studies of electron neutrino and

muon neutrino charged current, quasi-elastic events, can also be applied, slightly improving the electron and muon energy reconstruction accuracy [15]. Third, neutral pion invariant mass obtained from the opening angle and energy of the two measured decay photons provides another cross-check on the detector energy scale; typical reconstructed invariant masses are in good agreement with the well-known π^0 mass [Raaf:2004ty]. Fourth, the neutrino energy can be estimated in charged-current, quasi-elastic interactions from the energy and direction of the outgoing charged lepton. The expected neutrino energy reconstruction accuracy as obtained from Monte Carlo studies is described in the next Chapter, discussing muon neutrino charged-current, quasi-elastic interactions in MiniBooNE.

Finally, the calibration constants relating the Cherenkov and scintillation light fluxes to energy, that is the constants C_ρ and C_ϕ appearing in Tab. 6.2, are obtained from electrons from muon decays at rest [10].

6.3.3 Particle identification

Particle identification in MiniBooNE aims at distinguishing events with a muon, electron, or a neutral pion in the final state. Qualitatively, muon events are characterized by single, long tracks slowing down and brought to rest in the detector because of ionization energy loss, with little scattering along the path. Electron events are characterized by single, shorter tracks, whose development is affected by electron bremsstrahlung and ionization, and by photon pair production and Compton scattering. Since typical electron energies (tens to few hundreds of MeV) are of the order of the electron critical energy in mineral oil. Therefore, in the MiniBooNE energy regime, electrons do not behave neither as minimum ionizing particles, nor as electromagnetic showers, but rather as something in between. The result is that the Cherenkov light ring emitted by electrons is not as filled in as for muon tracks (because of the shorter track lengths), and with a fuzzier ring profile (because of

its partially “shower-like” properties). Neutral pion events are characterized by two electron-like Cherenkov rings, from the conversion of the two photons from $\pi^0 \rightarrow \gamma\gamma$ decays.

For example, electron/muon separation is accomplished using [17]:

- the number of decay electrons in the event;
- functions depending on reconstructed physical observables, for example the ratio of track length to energy;
- charge related quantities, possibly functions of both the reconstructed and predicted PMT charges, or depending only on PMT reconstructed charges, as a function of various topological variables. A first example involving only reconstructed charges is the distribution of charge as a function of the angle between the track direction and the direction defined by the PMT locations with respect to the track midpoint; muon-like tracks are more extended, and tend to have broader distributions in this angular variable. A second example is the distribution of charge per unit track length along the track, assuming that all photons are emitted at an angle equal to the Cherenkov angle with respect to the track direction; muon-like tracks, with a nearly uniform light production per unit track length and sharply-defined Cherenkov rings, tend to have a narrow distribution in this quantity. One example using both reconstructed and predicted charges is the value of the charge likelihood \mathcal{L}_q appearing in Tab. 6.2;
- distributions related to PMT corrected times, such as the time likelihood \mathcal{L}_t appearing in Tab. 6.2, possibly as a function of the same topological variables discussed above;
- distributions related to both PMT charges and times, possibly as a function of the same topological variables discussed above.

Several variants on these quantities are used, and the distributions predicted by the reconstruction algorithms under various reconstruction assumptions, are exploited.

The goal of this analysis is to study $\nu_\mu n \rightarrow \mu^- p$ interactions. As discussed in the next Chapter, the main background to this analysis are muon neutrino, charged-current interactions where a single pion is also produced. Both event typologies have (at least) one muon in the final state and no prompt electrons. As it will be explained in detail later, similar tools to the ones listed above for electron/muon separation are used in this case, but tailored to the different signal/background event classification.

Reconstruction Step	1	2	3	4
Negative logarithm of time likelihood \mathcal{L}_t	$-\sum_i \ln P(t_{\text{corr},i}(\vec{x}, t))$	$-\sum_i \ln P(t_{\text{corr},i}(\vec{x}, t); E_1, \mu_i(\rho_1, E_1, \phi_1, \vec{x}, \vec{u}))$	$-\sum_i \ln P(t_{\text{corr},i}(\vec{x}_2, t_2); E_1, \mu_i(\rho, E_1, \phi, \vec{x}_2, \vec{u}_2))$	$-\sum_i \ln P(t_{\text{corr},i}(\vec{x}_2, t_2); E_3, \mu_i(\rho_3, E_3, \phi_3, l, \vec{x}_2, \vec{u}_2))$
Negative logarithm of charge likelihood \mathcal{L}_q		$-\sum_j \ln P(q_j; \mu_j(\rho_1, E_1, \phi_1, \vec{x}, \vec{u}))$	$-\sum_j \ln P(q_j; \mu_j(\rho, E_1, \phi, \vec{x}_2, \vec{u}_2))$	$-\sum_j \ln P(q_j; \mu_j(\rho_3, E_3, \phi_3, l, \vec{x}_2, \vec{u}_2))$
Track midpoint position \vec{x} and time t	(\vec{x}_1, t_1) from $-\ln \mathcal{L}_{t1}$ min.	(\vec{x}_2, t_2) from $-(\ln \mathcal{L}_{t2} + \ln \mathcal{L}_{q2})$ min.		
Track direction \vec{u}	$\vec{u}_1 = \vec{u}(q_i, t_i; \vec{x}_1, t_1)$	\vec{u}_2 from $-(\ln \mathcal{L}_{t2} + \ln \mathcal{L}_{q2})$ min.		
Track length l				l from $-(\ln \mathcal{L}_{t4} + \ln \mathcal{L}_{q4})$ min.
Cherenkov flux ρ	$\rho_1 = C_\rho E_1$		ρ_3 from $-(\ln \mathcal{L}_{t3} + \ln \mathcal{L}_{q3})$ min.	
Scintillation flux ϕ	$\phi_1 = C_\phi E_1$		ϕ_3 from $-(\ln \mathcal{L}_{t3} + \ln \mathcal{L}_{q3})$ min.	
Energy	$E_1 = E(Q; \vec{x}_1)$	$E_2 = E(Q, \vec{x}_2)$	$E_3 = \rho_3 / C_\rho$	

Table 6.2: Summary of the event reconstruction algorithm in MiniBooNE. See text for details. Table notation: i, j subscripts index PMTs with non-zero charge and all PMTs, respectively; \vec{x}_i is the PMT location; $t_{\text{corr},i}$ and q_j is the reconstructed PMT corrected time and charge, respectively; μ_j is the PMT charge predicted by the reconstruction algorithm; Q is the total charge, summed over all PMTs; c_n is the speed of light in a medium with refractive index n ; C_ρ and C_ϕ are constants; 1, 2, 3, 4 subscripts index the reconstruction step number; $\vec{x}, t, \hat{u}, \rho, \phi, l$ quantities appearing with no step number subscript are varied in the minimization step.

Bibliography

- [1] S. Eidelman *et al.* [Particle Data Group Collaboration], Phys. Lett. B **592**, 1 (2004).
- [2] I. Stancu *et al.* [MiniBooNE collaboration], “The Miniboone Detector Technical Design Report,” FERMILAB-TM-2207;
- [3] R. L. Imlay *et al.*, “Study of the Angular Reconstruction of Muons in MiniBooNE Using the Muon Tracker”, BooNE Technical Note 99 (2003);
- [4] R. L. Imlay *et al.*, “Measuring the Energy of Muons in MiniBooNE with the Cubes”, BooNE Technical Note 106 (2004);
- [5] H. H. Meyer, “Index of Refraction of Marcol 7”, BooNE Technical Note 90 (2003);
- [6] B. C. Brown *et al.* [the MiniBooNE collaboration], “Study of scintillation, fluorescence and scattering in mineral oil for the MiniBooNE neutrino detector,” FERMILAB-CONF-04-282-E; *Prepared for 2004 IEEE Nuclear Science Symposium and Medical Imaging Conference (NSS / MIC), Rome, Italy, 16-22 Oct 2004*
- [7] A. O. Bazarko *et al.*, “Studies of Scattering in Marcol 7 Mineral Oil”, BooNE Technical Note 144 (2004);

- [8] The technical specifications for the Hamamatsu R5912 photomultiplier tube can be downloaded from:
<http://www.datasheetarchive.com/HamamatsuCorporation4.html>
- [9] R. B. Patterson, “The PMT Charge Calculation”, BooNE Technical Note 83 (2003);
- [10] Y. Liu and I. Stancu, “The MiniBooNE Charge Likelihoods and Light Scattering in Michel Electron Events”, BooNE Technical Note 126 (2004);
- [11] Y. Liu and I. Stancu, “Toward the MiniBooNE Charge Likelihood”, BooNE Technical Note 100 (2003);
- [12] I. Stancu, “The Single-PE Time Resolution with Ryan Patterson’s QT-Algorithms”, BooNE Technical Note 81 (2003);
- [13] I. Stancu, “An Introduction to the Maximum Likelihood Event Reconstruction in MiniBooNE”, BooNE Technical Note 50 (2002);
- [14] Y. Liu and I. Stancu, “In Situ Speed of Light Measurements at $\lambda=400$ nm and $\lambda=440$ nm”, BooNE Technical Note 125 (2004);
- [15] A. Aguilar-Arevalo, “Neutrino Energy Reconstruction Studies for numu Quasi-Elastic Events”, BooNE Technical Note 97 (2003);
- [16] J. L. Raaf [BooNE Collaboration], arXiv:hep-ex/0408015.
- [17] Y. Liu and I. Stancu, “The Performance of the S-Fitter Particle Identification”, BooNE Technical Note 141 (2004);